The OSIRIS instrument on the Odin spacecraft

E.J. Llewellyn, N.D. Lloyd, D.A. Degenstein, R.L. Gattinger, S.V. Petelina, A.E. Bourassa, J.T. Wiensz, E.V. Ivanov, I.C. McDade, B.H. Solheim, J.C. McConnell, C.S. Haley, C. von Savigny, C.E. Sioris, C.A. McLinden, E. Griffioen, J. Kaminski, W.F.J. Evans, E. Puckrin, K. Strong, V. Wehrle, R.H. Hum, D.J.W. Kendall, J. Matsushita, D.P. Murtagh, S. Brohede, J. Stegman, G. Witt, G. Barnes, W.F. Payne, L. Piché, K. Smith, G. Warshaw, D.-L. Deslauniers, P. Marchand, E.H. Richardson, R.A. King, I. Wevers, W. McCreath, E. Kyrölä, L. Oikarinen, G.W. Leppelmeier, H. Auvinen, G. Mégie, A. Hauchecorne, F. Lefèvre, J. de La Nöe, P. Ricaud, U. Frisk, F. Sjoberg, F. von Schéele, and L. Nordh

Abstract: The optical spectrograph and infrared imager system (OSIRIS) on board the Odin spacecraft is designed to retrieve altitude profiles of terrestrial atmospheric minor species by observing limb-radiance profiles. The grating optical spectrograph (OS) obtains spectra of scattered sunlight over the range 280–800 nm with a spectral resolution of approximately 1 nm. The Odin spacecraft performs a repetitive vertical limb scan to sweep the OS 1 km vertical field of view over selected altitude ranges from approximately 10 to 100 km. The terrestrial absorption features that are superimposed on the scattered solar spectrum are monitored to derive the minor species altitude profiles. The spectrograph also detects the airglow, which can be used to study the mesosphere and lower thermosphere. The other part of OSIRIS is a three-channel infrared imager (IRI) that uses linear array detectors to image the vertical limb radiance over an altitude range of approximately 100 km. The IRI observes both scattered sunlight and the airglow emissions from the oxygen infrared atmospheric band at 1.27 μm and the OH (3-1) Meinel band at 1.53 μm. A tomographic inversion technique is used with a series of these vertical images to derive the two-dimensional distribution of the emissions within the orbit plane.

PACS Nos.: 07.05.Pj, 07.60.Dq, 07.60.Rd, 07.87, 94.10.Dy, 94.10.Fa, 94.10.Gb, 94.10.Rk

Résumé : Le système de spectrographie optique et d'imagerie infrarouge (OSIRIS) à bord du satellite Odin est conçu pour enregistrer les profils en altitude des éléments mineurs de l'atmosphère en observant les profils de radiance du limbe. Le spectrographe optique à réseau (OS) obtient les spectres de la lumière solaire diffusée sur le domaine entre 280–800 nm, avec une résolution spatiale approximative de 1 nm. Le satellite Odin balaye verticalement le limbe de façon répétée, de telle sorte que l'ouverture verticale de 1 km du OS parcoure les domaines voulus entre 10 et 100 km. Nous analysons les spectres solaires diffusés en superposition avec les caractéristiques terrestres d'absorption, afin de déterminer les profils en altitude des éléments mineurs de l'atmosphère. Le spectrographe détecte aussi la luminescence nocturne atmosphérique qui peut être utilisé pour étudier la mésosphère et la thermosphère. L'autre partie d'OSIRIS est un imageur infrarouge (IRI) à trois canaux qui utilise une banque linéaire de détecteurs pour imager la radiance du limbe sur un domaine d'altitude d'approximativement 100 km. L'IRI observe à la fois la lumière solaire diffusée et les émissions de luminescence nocturne atmospérique provenant de la bande infrarouge de l'oxygène atmosphérique à 1.27 μm et la bande de Meinel de l'OH (3-1) à 1.53 μm. Nous utilisons une technique d'inversion tomographique avec une série de ces images verticales pour obtenir la distribution bidimensionnelle des émissions à l'intérieur de l'orbite.

[Traduit par la Rédaction]

1. Introduction

The Odin satellite was launched on 20 February 2001, from the Svobodny Cosmodrome in Eastern Siberia into a near circular Sun-synchronous orbit. The satellite serves a combined aeronomy/astronomy mission and includes only two instruments: the sub-mm/mm radiometer (SMR) and the optical spectrograph and infrared imager system (OSIRIS). The objective of the aeronomy mission is to provide new information on the extent to which humans are changing the atmospheric environment. This broad objective has been more clearly defined by Murtagh et al. [1] as:

1. Stratospheric ozone science: To elucidate the geographical extent of, and mechanisms responsible for, ozone depletion in the "ozone hole" region and to study dilution effects and possible heterogeneous chemistry even outside of the polar regions due to sulphate aerosols.

E.J. Llewellyn,[1] N.D. Lloyd, D.A. Degenstein, R.L. Gattinger, S.V. Petelina, A.E. Bourassa, J.T. Wiensz, and E.V. Ivanov. ISAS, Department of Physics and Engineering Physics, University of Saskatchewan, Saskatoon, SK S7N 5E2, Canada.
I.C. McDade[2] and J.C. McConnell[2]. EATS, York University, 4700 Keele Street, North York, ON M3J 1P3, Canada.
B.H. Solheim, C.S. Haley, C. von Savigny,[3] C.E. Sioris,[4] C.A. McLinden,[5] E. Griffioen, and J. Kaminski. CRESS, York University, 4700 Keele Street, North York, ON M3J 1P3, Canada.
W.F.J. Evans and E. Puckrin.[6] Physics Department, Trent University, Peterborough, ON K9J 7B8, Canada.
K. Strong. Physics Department, University of Toronto, 60 St. George Street, Toronto, ON M5S 1A7 Canada.
V. Wehrle, R.H. Hum, D.J.W. Kendall, and J. Matsushita.[7] Canadian Space Agency, Ottawa, ON K1A 0R6, Canada.
D.P. Murtagh and S. Brohede. Department of Radio and Space Science, Chalmers University of Technology, SE-412 96 Göteborg, Sweden.
J. Stegman and G. Witt. MISU, Department of Meteorology, Stockholm University, SE-106 91 Stockholm, Sweden.
G. Barnes, W.F. Payne, L. Piché, K. Smith, G. Warshaw[7], D.-L. Deslauniers, and P. Marchand. Routes AstroEngineering Ltd., 303 Legget Road, Kanata, ON K2K 3B1, Canada.
E.H. Richardson.[8] EHR Optical Systems, 1871 Elmhurst Pl., Victoria, BC V8N 1R1, Canada.
R.A. King[9] and I. Wevers. Physics and Astronomy Department, University of Calgary, Calgary, AB T2N 1N4, Canada.
W. McCreath. WavePrecision Inc., Nepean, ON K2E 7Y8, Canada.
E. Kyrölä, L. Oikarinen[7], G.W. Leppelmeier,[10] and H. Auvinen. Finnish Meteorological Institute, Geophysical Research, P.O. Box 503, FIN-00101 Helsinki, Finland.
G. Mégie, A. Hauchecorne, and F. Lefèvre. Service d'Aeronomie, Institut Pierre-Simon Laplace, Jussieu, Paris, France.
J. de La Nöe and P. Ricaud. Observatoire Aquitain des Sciences de l'Univers, Laboratoire d'Astrodynamique, d'Astrophysique et d'Aéronomie de Bordeaux, Floirac, France.
U. Frisk, F. Sjoberg, and F. von Schéele. Swedish Space Corporation, Albygatan 107, Solna, SE-171 04, Sweden.
L. Nordh. Swedish National Space Board, Albygatan 107, Solna, SE-171 04, Sweden.

[1] Corresponding author (e-mail: edward.llewellyn@usask.ca).
[2] Also at: CRESS, York University, 4700 Keele Street, North York, ON M3J 1P3, Canada.
[3] Also at: IUP/IFE, University of Bremen, D-28359 Bremen, Germany.
[4] Also at: SAO, Harvard University, 60 Garden Street, Cambridge, MA 02138, U.S.A.
[5] Also at: MSC, Environment Canada, 4905 Dufferin Street, Downsview, ON M3H 5T4, Canada.
[6] Also at: Defence R&D Canada - Valcartier, Val-Bélair, QC G3J 1X5, Canada.
[7] Deceased.
[8] Also at: University of Victoria, Victoria, B.C. V8W 3P6, Canada.
[9] Now at: Lunar and Planetary Laboratory, University of Arizona, Tucson, AZ 85721, U.S.A.
[10] Also at: G & S Associates, Yläkaupinkuja 2, 02360 Espoo, Finland.

2. Mesospheric ozone science: To establish the relative role of odd hydrogen chemistry and the effects of ordered and turbulent transport and corpuscular radiation.

3. Summer mesosphere science: To establish the variability of mesospheric water vapour including an assessment of the required fluxes for aerosol formation in the polar mesosphere, i.e., polar mesospheric clouds.

4. Coupling of atmospheric regions: To study some of the mechanisms that provide coupling between the upper and lower atmosphere, e.g., downward transport of aurorally enhanced NO with its effects on ozone photochemistry and the vertical exchange of minor species such as odd oxygen, CO, and H_2O.

To meet these scientific goals the satellite, which is in a circular Sun-synchronous orbit at 600 km with the ascending node at 1800 Local Time (LT), is pointed at the limb, usually in the direction of the satellite track, and the entire satellite nodded so that the co-aligned optical axes of the radiometer and OSIRIS sweep over selected altitude ranges, between approximately 10 and 100 km. The entrance slit for the OS is aligned parallel to the horizon, while the three one-dimensional array detectors in the IRI are aligned perpendicular to the horizon.

The OS data include two types of information, Rayleigh-scattered sunlight spectra containing atmospheric absorption features within the wavelength range 280–800 nm and atmospheric emission features, including the airglow from sodium and molecular oxygen plus numerous auroral emissions. For the scattered solar spectra the Sun acts as a light source against which absorption by lines and diffuse bands of species such as ozone and NO_2 can be measured, and hence column abundances inferred. The IRI data are also of two types, Rayleigh-scattered sunlight and the airglow, although in these cases the spectral selection is achieved with interference filters so that individual absorption features cannot be studied.

In this paper, the approach to the basic OSIRIS design and the on-orbit performance evaluation are presented. Preliminary reports on the OSIRIS concept have been presented elsewhere [2, 3]. While the concept of limb scanning is not new, the tomographic approach used with the IRI represents a major advance and the new opportunities afforded by this novel approach to limb imaging are also briefly discussed.

2. The optical spectrograph and infrared imaging system (OSIRIS)

An example of the expected (pre-flight) on-orbit scattered limb spectra, calculated using the MOD-TRAN code, is shown in Fig. 1*a* while examples of the first observed limb spectra are shown in Fig. 1*b*. The obvious data gap in Fig. 1*b* is intentional; it is in the region of the order sorter where the spectrum is not recorded. The general decrease in the scattered intensity below 330 nm, which is apparent in both Figs. 1*a* and 1*b*, is due to Rayleigh extinction as well as ozone absorption. The broad absorption feature near 600 nm is also due to ozone and the narrow absorption feature at 762 nm is due to the (0–0) band of the oxygen atmospheric absorption system ($b^1\Sigma_g^+ \Leftarrow X^3\Sigma_g^-$). It should be noted that the water vapour and O_2 B-band, the (1–0) transition of the oxygen atmospheric absorption system, absorptions that are evident in Fig. 1*b* at "high" altitudes are really an albedo signature and do not imply that there is absorption by these features at these high tangent altitudes. It is readily apparent that there is excellent agreement between the preflight expected spectra and those actually observed, this implies that the on-orbit performance of OSIRIS is very close to that predicted.

3. The optical spectrograph (OS)

The OSIRIS instrument is shown schematically in Fig. 2. As already noted for normal operation, the instrument is pointed at the limb so that scattered light from the terrestrial limb enters the OS (Fig. 2) through the baffle section of the telescope. As OSIRIS and the SMR, which are co-aligned, are pointed at the limb for normal aeronomy operation the bright Earth is always very close to the optical axis so that rejection of off-axis scattered light is paramount for satisfactory instrument performance.

Fig. 1. (*a*) Typical preflight on-orbit limb spectra calculated using the MODTRAN code for high-latitude winter conditions, convolved with a 1 nm slit function. Radiance units are 10^6 photons/Å/4π. The sharp absorption features at 690 and 760 nm are due to molecular oxygen while the broad feature centred around 600 nm is due the Chappuis bands of ozone. (*b*) An early mission limb image sequence obtained with the optical spectrograph when Odin was near 80° N. The altitude range of the tangent line of sight of the scan is between approximately 10 and 60 km. The radiance units correspond to 10^6 photons/Å/4π
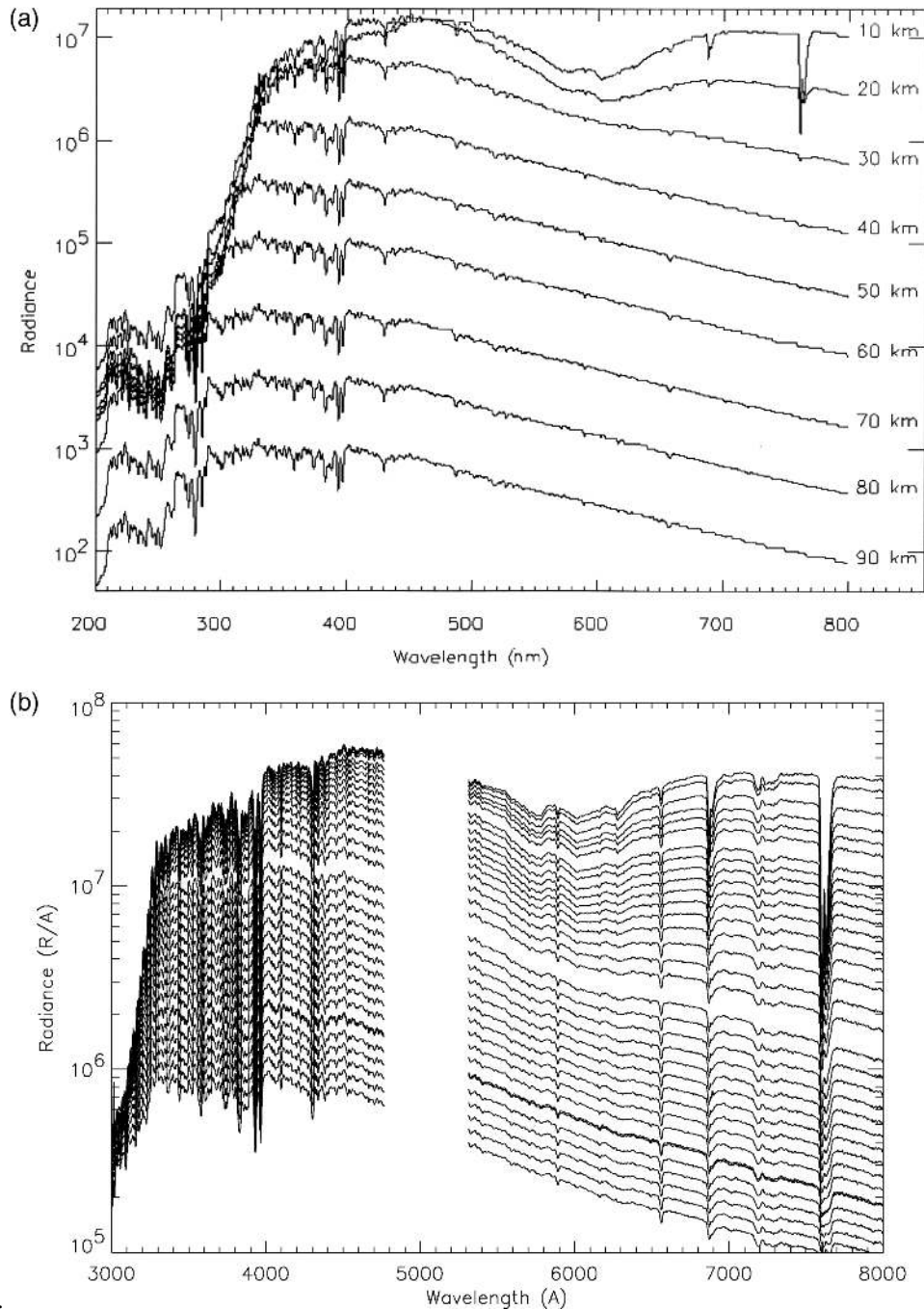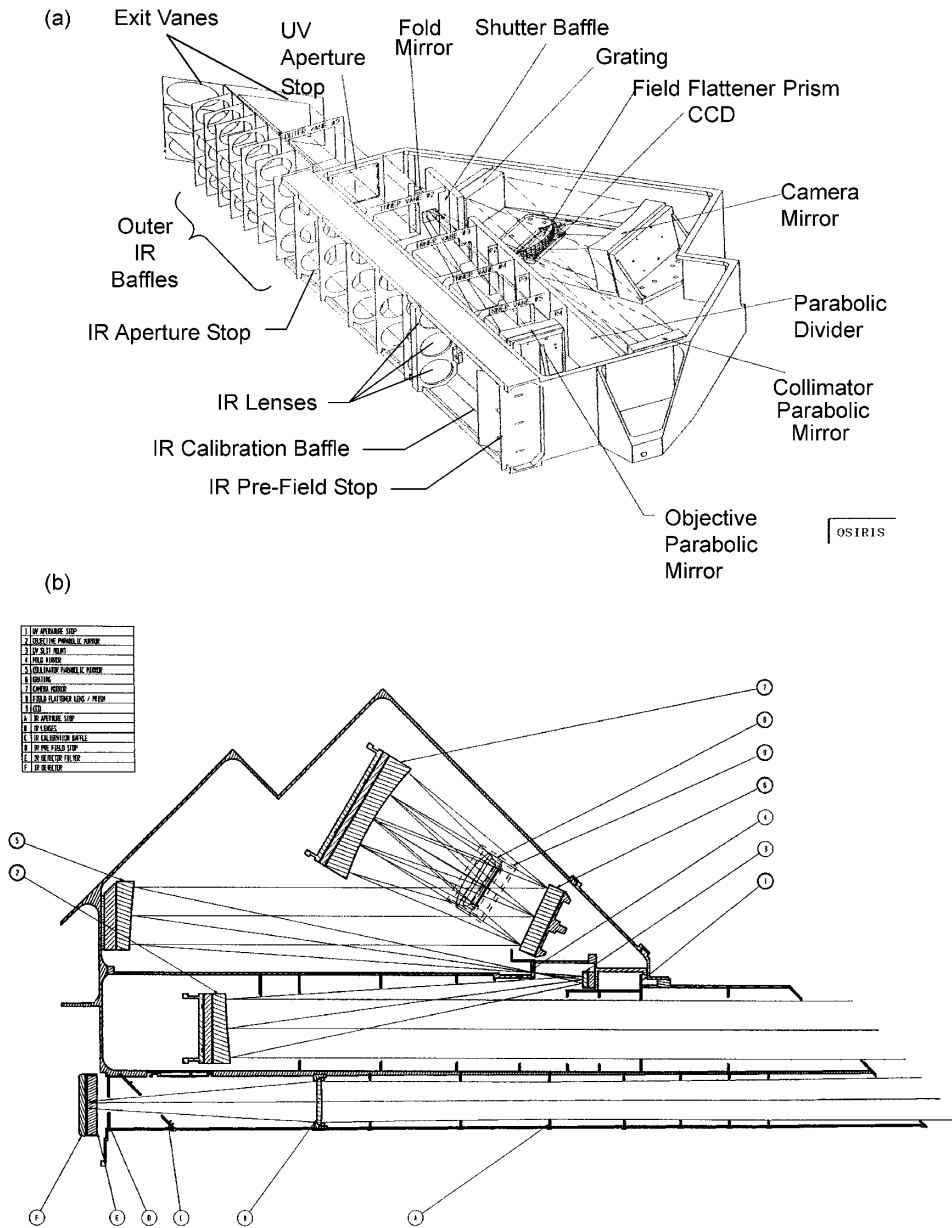
Fig. 2. (*a*) A schematic of the optical spectograph (OS) and infrared imager (IRI) illustrating the mechanical layout. (*b*) A schematic of the optical layout in OSIRIS.

The OS baffle characterization and its on-orbit performance is discussed in more detail in Appendix A. The telescope mirror is an off-axis parabolic mirror, focal length approximately 250 mm, effective size 36 mm by 36 mm, that forms an image of the limb on the slit; the 90 μm wide entrance slit is oriented horizontally. The resultant vertical field of view at the limb tangent point is approximately 1 km; the slit length corresponds to approximately 20 km (horizontal) at the limb. The fold mirror just before the slit serves to reduce the overall dimensions of the instrument. A fail-open shutter is located immediately behind the slit.

Inside the spectrograph the first optical element is the collimating mirror, an off-axis parabolic that matches the telescope mirror. The collimated beam is then incident on the 600 grooves/mm grating

Fig. 3. Optical spectrograph sensitivity plot measured prelaunch.
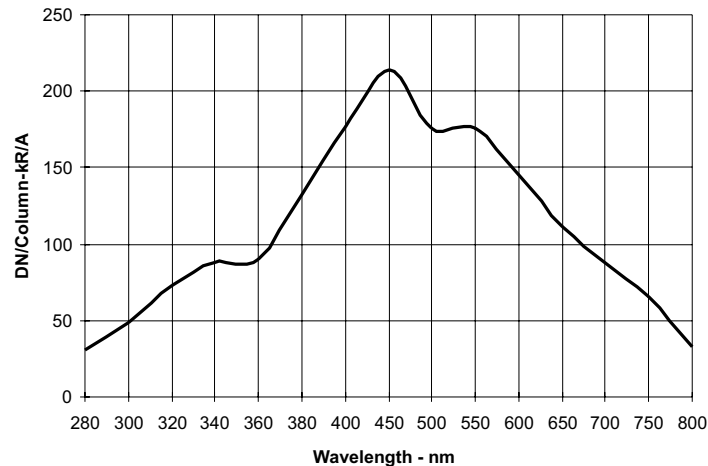
(blazed at 400 nm), provided by Instruments SA/Jobin-Yvon. This specialized grating is designed to be slightly aspheric to compensate for aberrations in the spherical camera mirror. All mirror surfaces are protected with a SiO_2 overcoating. The effects of grating polarization, which were measured during the prelaunch characterization, have been discussed by McLinden et al. [4]. The 45° internal reflection prism redirects the beam from the camera mirror on to the out-of-plane detector. The detector is an EEV CCD, Model CCD26, operated in frame transfer MPP mode and selected for good quantum efficiency, low noise, and a minimum number of bad pixels. The spectral response covers the desired wavelength range from 280 to 800 nm. A spectral resolution of approximately 1 nm is achieved throughout the wavelength range using the 1353 pixels in a CCD row. The spectral point spread function and the wavelength calibration of the spectrograph were measured during the OSIRIS preflight characterization using a number of spectral line emission sources. In flight the wavelength calibration is automatically recorded with the Fraunhofer features in the sky spectrum. As Odin is flying in a terminator orbit, 1800 LT ascending node, the thermal environment of the spacecraft is relatively constant. However, during the northern hemisphere summer solstice the satellite does experience eclipse, this results in a decrease of the temperature of the optical bench in the OS. One consequence of this temperature change is a defocusing of the spectral image and a significant loss of resolution until the OS recovers its normal operating temperature. This temperature effect has been minimized through the use of a small heater mounted directly under the optical bench. An imaging capability along the slit, 32 rows on the CCD, is also included to enable observations of horizontal structure at the terrestrial limb. The exposure times range from 10 ms to 10 s. The CCD is maintained at a temperature that varies during the course of the year between approximately −25 and −10 °C by passive cooling, the temperature variation is caused by the change in the β angle, the angle between the Sun and the normal to orbital plane, and the consequent variation in power produced by the solar panels. At these detector temperatures, the dark current is always a very minor fraction of the total signal. There is an advantage to the use of passive cooling, beyond the obvious one of power saving, as each time Odin is switched to the astronomy mode so the detector is warmed and any condensation removed. However, it should be noted that there is no obvious icing of the cooled detectors.

It is readily apparent from the preflight calculated data, Fig. 1*a*, that the low-tangent altitude observations at wavelengths near 300 nm are particularly susceptible to contamination from the very bright visible region signals. Thus, it is important that the spectrograph was designed to minimize the effects of spectral cross-talk. In this respect, the most important optical component in the OS is the 45° prism, this also includes field-flattening lenses that are bonded on to the surface and an order-sorting colored glass filter. The basic Ebert–Fastie spectrograph design [5], and the Czerny–Turner variation, suffers from a high degree of spectral cross-talk and it is common to use two spectrometers in series to reduce this effect [6]. The limited space available on the Odin satellite precluded this approach and the same

performance was achieved with the 45° prism. Light from the spectrograph walls that reaches the prism has a large angle of incidence and so is reflected with a high efficiency and not transmitted to the detector. OSIRIS also differs from these other designs in that it uses a spherical, tilted camera mirror and an aspherized grating spectrograph, as for the CFHT [7], but again differs in that for OSIRIS the grating is off-axis [8]. In addition, despite being off-axis perpendicular to dispersion, the spectrograph is designed so that the spectral lines are not tilted and thus can be binned. With this optical layout and the selection of coating materials that provide low bi-directional reflectance distribution function (BRDF) values the internal scattered light level in the OS is very low, it is better than 5×10^{-6} in the ultraviolet region. This value was determined from measurements of the ultra-violet spectral response, with a series of short-wave cut-off filters, to a quartz halogen source.

The OS system sensitivity as a function of wavelength, summed over 32 rows, is shown in Fig. 3. This sensitivity was measured during the OS calibration and characterization phase with a number of different calibrated sources. However, as part of the general monitoring of the OS performance during the period between OSIRIS delivery to Sweden for integration into the spacecraft (May 1998) and shipping to the launch site (January 2001) full frame images of various sources were collected on an irregular basis. It became apparent in late 2000 that the full frame image, see Fig. 4, exhibited significant structure that could potentially impact the mission data. As the OS slit is in the focal plane of the telescope mirror it was possible to inspect the slit with an astronomical telescope that was directed toward the OS telescope mirror and focused at infinity, without dismantling the OS. This slit inspection just prior to launch indicated a slight deposit of unidentified material; this is most probably from the adhesive used with the field flattener on the 45° prism, but it has not significantly degraded instrument performance. Measurements of the post-launch sensitivity, based on the atmospheric limb Rayleigh-scattered-light signal, agree with prelaunch sensitivity to better than 20% over the entire wavelength range of the signal. In flight, the full slit image is continuously monitored for any change in the deposited material by including data from seven full CCD columns in place of the data omitted in the order-sorter region.

The noise in the on-orbit detected signals is limited by photon-counting statistics, the contribution from the electronics chain is approximately 1 DN (digitization number), which is essentially insignificant. 1 DN corresponds to approximately 13 CCD electrons.

Typical OS spectra for various limb altitudes are shown in Fig. 1b. As already noted, these observed spectra are generally in good agreement with the MODTRAN model values shown in Fig. 1a. A number of spectral fitting techniques including the method described by Flittner et al. [9] and implemented by von Savigny et al. [10, 11] as well as the differential optical absorption spectroscopy (DOAS) method [12–15] that is currently used to analyze GOME satellite data [16] are being used to derive vertical limb profiles of the relevant atmospheric species. These profiles [17], now available over the sunlit hemisphere, provide valuable inputs to global three-dimensional models. As there is a limited on-board storage for the OSIRIS data the OS controller collapses the 32 rows of the CCD into a single output row; this may be done through either on- or off-chip binning. However, even this procedure does not provide sufficient data compression nor ensure optimal signal to noise for the collected spectra. This is in fact achieved by using an automatic exposure algorithm that yields spectra with a typical count of 8000 DN, the maximum count is 16383 DN, and a data throttle that ensures the available memory is not filled before the next data downlink at Esrange in northern Sweden.

The OS is sufficiently sensitive that it is possible to make auroral observations when the atmosphere is not illuminated and the optical axis of the spectrograph is tangent to the limb in the upper mesosphere. An example of such a spectrum acquired early in the mission is shown in Fig. 5. The emissions at 391.4 and 427.8 nm, the (0,0) and (0,1) bands of the N_2^+ First Negative System ($B^2\Sigma_u^+ \Rightarrow X^2\Sigma_g^+$), as well as the atomic oxygen lines at 297.2, 557.7, and 630 nm are all clearly apparent and provide a valuable check on the relative response of the spectrograph. The feature around 762 nm is a blend of the (3,1) band of the N_2 First Positive ($B^3\Pi_g \Rightarrow A^3\Sigma_u^+$) System and the (0,0) band of the Oxygen Atmospheric ($b^1\Sigma_g^+ \Rightarrow X^3\Sigma_g^-$) System. This blending clearly illustrates the difficulty in trying to determine the auroral height profile of the oxygen emission with a simple rocket-borne filter photometer [18].

Fig. 4. False colour full-frame image showing the obvious structure associated with the OS slit.
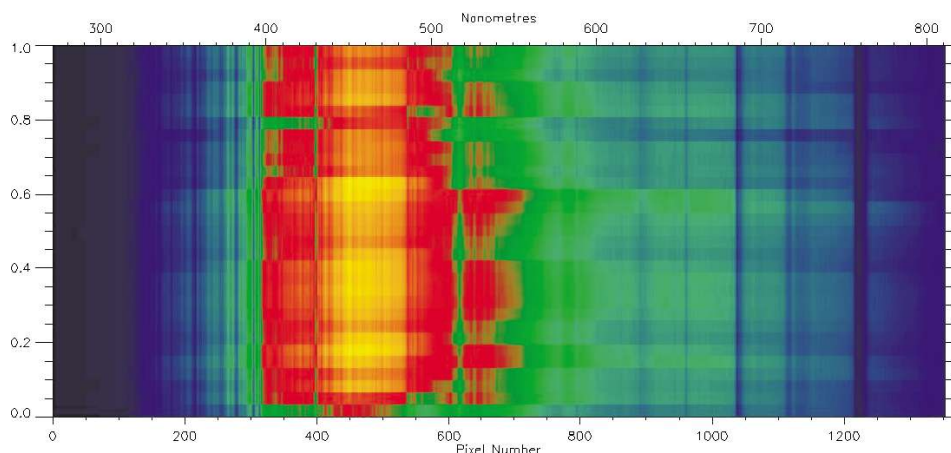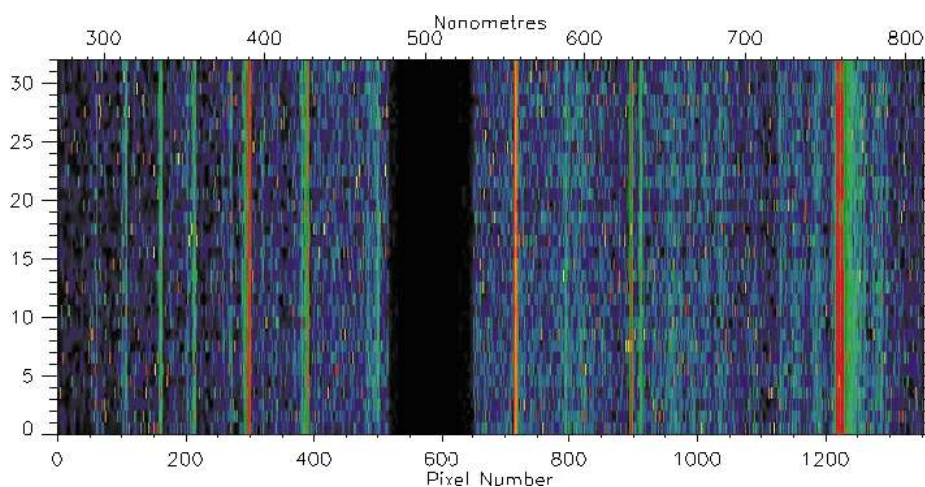

Fig. 5. Spectrograph image obtained over Antarctica with the OSIRIS line of sight fixed at a tangent altitude of 80 km. The obvious auroral features and the blending of the oxygen A-band with the N_2 1 PG feature is readily apparent. The absence of data in the region centered around 500 nm is due to the order sorter.

4. The infrared imager (IRI)

The IRI part of OSIRIS, also shown in Fig. 2, is actually three separate co-aligned single lens interference filter imagers operating at 1.263, 1.273, and 1.530 μm. The first two channels are intended primarily to map the molecular oxygen infrared atmospheric band emission (a $^1\Delta_g - X^3\Sigma_g^-$) in the orbit plane. This airglow feature is excited in the daytime through the photolysis of ozone, so that the measured limb profiles lead directly to ozone density profiles. The purpose of using two channels to detect the infrared atmospheric band, each channel has a different band capture fraction, is to provide both redundancy and an improved correction for the absorption along the line-of-sight [19]. The 1.530 μm imager observes both Rayleigh- and aerosol-scattered sunlight and the (3–1) OH Meinel vibration–rotation band airglow. The required vertical airglow profiles are obtained from a tomographic inversion of the measured limb profiles [19, 20].

Each channel has a light baffle, a combined shutter and calibration source, a simple zinc selenide lens (the IR lenses are telecentric with a specially applied AR coating to reduce rms surface roughness), as well as an optical interference filter and a Sensors Unlimited InGaAs (Model SU128L) 128 element

Fig. 6. (*a*) A false colour plot of the twilight and nighttime image sequence for the 1.27 μm imager channel. (*b*) A false colour image showing the variation of the oxygen infrared atmospheric band emission profile along the orbit track.
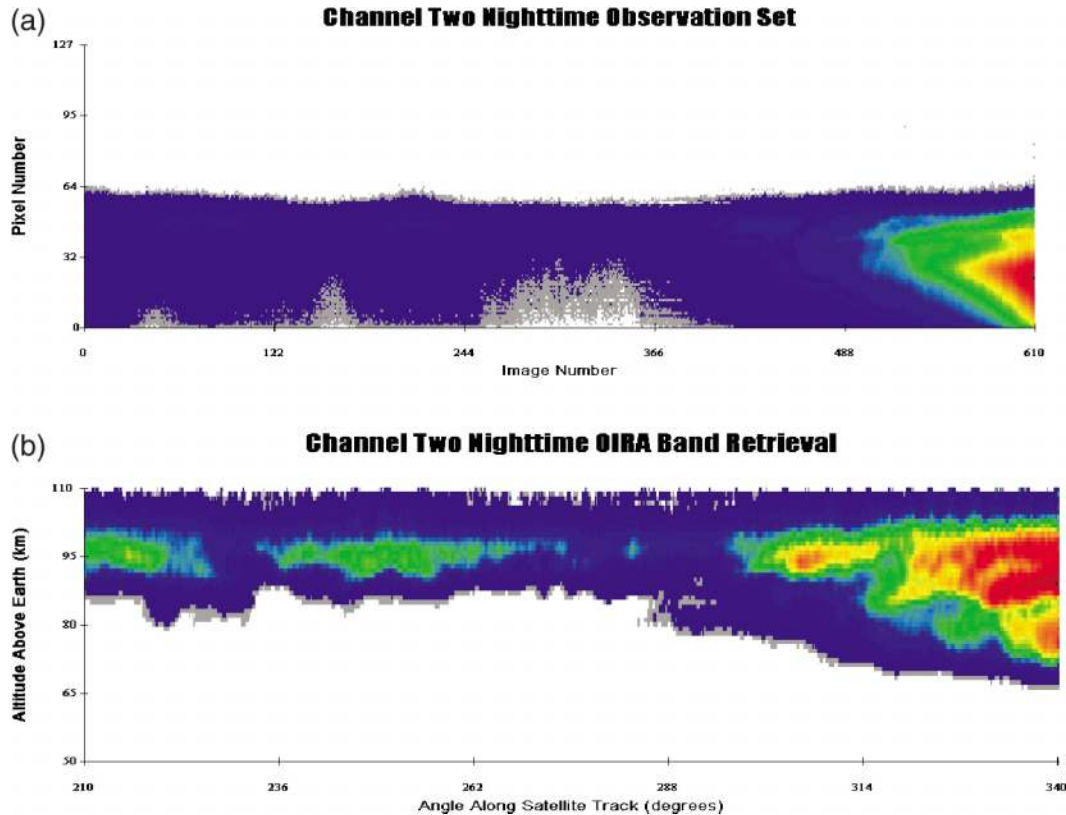

Table 1. IRI prelaunch calibration — units are photons/cm^2 4π sterad nm s for 1 DN.

1.263μ	1.273μ	1.530μ
4500 R/nm DN	4100 R/nm DN	1400 R/nm DN

linear array. The lens diameter is 23 mm and has a focal length of approximately 50 mm. The vertical field of view for each channel is approximately 100 km with the IRI lower altitude limit located approximately 10 km below the OS boresight. The detector dark current is continuously monitored through the use of masked pixels at one end of each thermoelectrically cooled array. The interference filters are mounted directly on to the thermoelectric housing and so are also cooled with the result that the passbands are shifted from their room temperature values. Thus the calibration and characterization were made at a number of temperatures so that any changes in the filter passbands due to temperature change could be corrected. The short wavelength filters have nearly Gaussian passbands while the long wavelength channel has a square passband. As part of the calibration procedures the passbands were carefully checked for out-of-band rejection. The prelaunch calibration results of the three IRI channels, expressed as a typical single-pixel response, are given in Table 1 for each of the channels. The estimated noise floor in each channel is approximately 5 DN. The postlaunch calibration and noise levels are in good agreement with the prelaunch values. One point that should be noted about an imaging instrument is that it is really many instruments, equal to the number of pixels, and that the characterization and calibration must recognize this fact.

As with the OS, stray light from bright off-axis signals are present in the observed signal; at the highest altitudes the scattered-light signal can exceed the true signal. There has been extensive analysis of the stray light effects [21] in the imager and preflight estimates of stray light rejection are in good agreement with the observed on-orbit performance [22]. The in-flight data are corrected for the scattered light levels on each array before the measurements are used with the developed data analysis algorithms. In actual flight operation, the IRI is independent of the OS and makes 1 s exposures every 2 s. To optimize the tomographic procedures the satellite is operated in a stare mode, i.e., the IRI optic axis is held at a fixed tangent altitude for one entire orbit each aeronomy observation day. In normal operation, the satellite nods to provide the required limb scans for OS and the radiometer, although this complicates the tomographic analysis.

The tomographic analysis procedures have been discussed by a number of authors [19, 20, 23–26] and the reader is directed to those works for the details. An example of an early mission observation of the limb profiles and the tomographic retrievals for the oxygen infrared atmospheric band in the twilight and nighttime portions of an orbit is shown in Fig. 6. The long evening decay of the emission is clearly apparent while spatial structures in the nighttime emission are also seen. However, perhaps the most striking feature of these observations is the structure associated with the twilight airglow; it is obviously far more complicated and detailed than that observed with a rocket photometer [27, 28]. Indeed this difference between the limb profiles and the retrievals clearly illustrates the gross smoothing that is introduced with an "onion-peel" type inversion. The analysis of these airglow structures with the tomographic technique is the key to the major scientific contributions that are being provided by the IRI observations.

5. Conclusions

It has been shown from a comparison of the preflight and in-orbit performance that the design goals of OSIRIS, both the optical spectrograph and the infrared imager components, have been achieved. While the detailed scientific analysis is only just beginning it is clear that the data being collected in the Odin mission are of excellent quality. These data will provide new opportunities to investigate, among other things, atmospheric species profiles, spatial structures, and dynamics.

Acknowledgements

References

1. D. Murtagh, U. Frisk, F. Merino, M. Ridal, A. Jonsson, J. Stegman, G. Witt, P. Eriksson, C. Jiménez, G. Mégie, J. de la Nöe, P. Ricaud, P. Baron, J.R. Pardo, A. Hauchcorne, E.J. Llewellyn, D.A. Degenstein, R.L. Gattinger, N.D. Lloyd, W.F.J. Evans, I.C. McDade, C.S. Haley, C. Sioris, C. von Savigny, B.H. Solheim, J.C. McConnell, K. Strong, E.H. Richardson, G.W. Leppelmeier, E. Kyrölä, H. Auvinen, and L. Oikarinen. Can. J. Phys. **80**, 309 (2002).
2. G.D. Warshaw, D.-L. Deslauniers, and D. Degenstein. Optical design and performance of the Odin UV/visible spectrograph and infrared imager instrument, 10th Annual AIAA/USU Small Satellite Conference, Logan, Utah. 1996.
3. E.J. Llewellyn, D.A. Degenstein, I.C. McDade, R.L. Gattinger, R. King, R. Buckingham, E.H. Richardson, D.P. Murtagh, W.F.J. Evans, B.H. Solheim, K. Strong, and J.C. McConnell. OSIRIS — an application of tomography for absorbed emissions in remote sensing. Applications of Photonic Technology 2, *Edited by* G.A. Lampropoulos and R.A. Lessard. Plenum Press, New York. 1997. pp. 627–632.

4. C.A. McLinden, J.C. McConnell, K. Strong, I.C. McDade, R.L. Gattinger, R. King, B. Solheim, E.J. Llewellyn, and W.J.F. Evans. Can. J. Phys. **80**, 469 (2002).
5. W.G. Fastie. J. Opt. Soc. Am. **42**, 641 (1952).
6. D.J. McEwen and P. Chakrabaty. Adv. Space Res. **2**(5), 209 (1982).
7. G.R. Lemaitre. Astron. Astrophys. **59**, 249 (1977).
8. G.R. Lemaitre and E. Harvey Richardson. SPIE, **3355**, 682 (1998).
9. D.E. Flittner, P.K. Bhartia and B.M. Herman. Geophys. Res. Lett. **27**, 2601 (2000).
10. C. von Savigny. Ph.D. thesis, York University. Toronto, Ont. 2002.
11. C. von Savigny, C.S. Haley, C.E. Sioris , I.C. McDade, E.J. Llewellyn, D. Degenstein, W.F.J. Evans, R.L. Gattinger, E. Griffoen, N. Lloyd, J.C. McConnell, C.A. McLinden, D.P. Murtagh, B. Solheim, and K. Strong. Geophys. Res. Lett. **30**(14), 1755, doi:10.1029/2002GL016401, (2003).
12. I.C. McDade, K. Strong, C.S. Haley, J. Stegman, D.P. Murtagh, and E.J. Llewellyn. Can J. Phys. **80**, 395, (2002).
13. C.E. Sioris, C.S. Haley, C.A. McLinden, C. von Savigny, I.C. McDade, J.C. McConnell, W.F.J. Evans, N.D. Lloyd, E.J. Llewellyn, K.V. Chance, T.P. Kurosu, D. Murtagh, U. Frisk, K. Pfeilsticker, H. Bösch, F. Weidner, K. Strong, J. Stegman, and G. Mégie. J. Geophys. Res. **108**(D7), 4215 (2003); doi:10.1029/2002JD002672.
14. C.S. Haley, C. von Savigny, S. Brohede, C.E. Sioris, I.C. McDade, E.J. Llewellyn, and D.P. Murtagh. Adv. Space Res. In press and available online at http://www.sciencedirect.com
15. K. Strong, B. Joseph, R. Dosanjh, I.C. McDade, C.A. McLinden, J.C. McConnell, J. Stegman, D.P. Murtagh, and E.J. Llewellyn. Can.J. Phys. **80**, 409 (2002).
16. J.P. Burrows, K.V. Chance, A.P.H. Goede, R. Guzzi, B.J. Kerridge, C. Muller, D. Perner, U. Platt, J.-P. Pommereau, W. Schneider, R.J. Spurr and H. van der Woerd. Global ozone-monitoring experiment: Interim science report. Report No. ESA SP-1151. *Edited by* T.D. Guyenne and C.J. Readings. ISBN 92-9092-041-6 European Space Agency, 1993.
17. OSIRIS on Odin web site. http://osirus.usask.ca. 2003.
18. I.C. McDade, E.J. Llewellyn and F.R. Harris. Can. J. Phys. **63**, 1322 (1985).
19. D.A. Degenstein. Ph.D. thesis, University of Saskatchewan, Saskatoon, Sask. 1999.
20. D.A. Degenstein, E.J. Llewellyn, and N.D. Lloyd. Appl. Opt. **41**, 1441 (2003).
21. E.V. Ivanov. M.Sc. thesis, University of Saskatchewan, Saskatoon, Sask. 2000.
22. A.E. Bourassa. M.Sc. thesis, University of Saskatchewan, Saskatoon, Sask. 2003.
23. N.D. Lloyd and E.J. Llewellyn. Can. J. Phys. **67**, 89 (1989).
24. I.C. McDade, N.D. Lloyd and E.J. Llewellyn. Planet. Space Sci. **39**, 895 (1991).
25. I.C. McDade and E.J. Llewellyn. Can. J. Phys. **69**, 1059 (1991).
26. I.C. McDade and E.J. Llewellyn. Can. J. Phys. **71**, 552 (1993).
27. W.F.J. Evans, D.M. Hunten, E.J. Llewellyn, and A.V. Jones. J. Geophys. Res. **73**, 2885 (1968).
28. W.F.J. Evans, I.C. McDade, J. Yuen, and E.J. Llewellyn. Can. J. Phys. **66**, 941 (1988).
29. C. Leinert and D. Kluppelberg. Appl. Opt. **13**, 556 (1974).

Appendix A. OS baffle performance

The intensity of the scattered sunlight at the limb of the Earth is strongly altitude dependent, thus the input telescope and baffle must be capable of rejecting large off-axis signals that can contaminate the true on-axis signals. Hence, a series simplified prelaunch baffle characterization tests were devised to measure the off-axis rejection ratios for the purpose of predicting on-orbit performance.

The bidirectional reflectance distribution function, $BRDF(\Theta)$, which is the ratio of scattered light radiance at off-axis angle Θ to the input irradiance, is defined as

$$BRDF(\Theta) = \frac{\text{Radiance}(\Theta)}{\text{Irradiance}} \text{ sr}^{-1} = \frac{P_S(\Theta)}{P_F \Omega_M} \text{ sr}^{-1}$$

where $P_S(\Theta)$ is the response per pixel from off-axis scattered light, P_F is the response per pixel with the source in the field of view, and Ω_M is the mirror solid angle subtended at the test source. All of these are directly measurable quantities.

Table A.1. UVIS baffle-scattered light contribution to in-field signal, expressed as a fraction of in-field signal.

Tangent height (km)	400 (nm)	550 (nm)	700 (nm)
25	0.0034	0.0055	0.024
40	0.018	0.034	0.14
70	0.65	1.1	4.4

The measured $BRDF(\Theta)$ of the spectrograph baffle, namely, the telescope mirror and the fold mirror that are the dominant scattering components in the baffle, was intermediate between the typical $BRDF(\Theta)$ for a freshly cleaned mirror and that for a slightly dusty mirror [29].

The integrated scattered light level, expressed as a fraction of the in-field signal, is given in Table A.1 for a number of wavelengths and for a number of limb tangent altitudes at a solar zenith distance of 80°. For the lower tangent heights and the shorter wavelengths the baffle contribution is minor, but for the longer wavelengths and the higher tangent heights the contribution from baffle-scattered light is much more serious.

The measured on-orbit baffle performance is in satisfactory agreement with the estimates shown in Table A.1. However, methods for the measurement and removal of baffle-scattered light using the in-flight data have been developed and are being applied to the collected observations. As a result, the scientific objectives are not seriously impacted by the effects of baffle scattered light.